

## 4. PARTICIPATION IN THE ASDEX UPGRADE PROGRAMME<sup>1</sup>

M.E. Manso and F. Serra (Heads), D. Borba, R. Coelho, L. Cupido, L. Fattorini, R. Galvão, S. Graça, L. Meneses, I. Nunes, V. Plyusnin, T. Ribeiro, F. Salzedas, J. Santos, A. Silva, F. Silva, P. Varela.

### 4.1. INTRODUCTION

The Portuguese participation in the ASDEX Upgrade<sup>2</sup> (AUG) programme has been mainly focused in two research lines:

- Microwave reflectometry;
- MHD, turbulence and transport.

### 4.2. MICROWAVE REFLECTOMETRY

#### 4.2.1. Introduction

This research line included in 2004 activities on microwave systems and electronics, control and data acquisition, data processing, diagnostic developments, modelling and plasma physics studies.

Concerning *microwave systems and electronics*, a new active frequency multiplier for the Q-band X-mode channel has been installed. A permanent marker switch has been implemented to provide dynamic calibration curves for all frequency sweeps every shot. All heterodyne channels have been tested and new IF filters with larger bandwidth have been installed for proper fast sweep operation. V-band X-mode channel was upgraded (new mixer and correction of default in antenna). Detailed dynamic frequency calibration circuit using a millimetre wave delay line (Figure 4.1) has been developed, to provide together with frequency markers a very accurate frequency calibration (Figure 4.2). A new in-vessel directional coupler at the Ka-band HFS channel has been installed, replacing the one damage by ECHR operation. New thermal and plasma protection for the waveguides (at LFS access port) were installed to avoid Halo currents in the waveguides. A vacuum window misalignment in the W-band LFS has been repaired.

Regarding *control and data acquisition*, control software of broadband channels has been optimized. It was modified after the installation of a new RS232 control boards to improve hardware control. New functionalities have been added to the broadband section: (i) new channels have been implemented to measure calibration signals; (ii) a logfile has been introduced to control eventual hardware faults; and (iii) software has been developed to switch on/off remotely each microwave source. Control software for a new “hopping” frequency system is being developed.

Concerning *data processing*, the burst mode data analysis for automatic density profile evaluation was validated with a 2D FDTD code. Software tools for automatic evaluation of the very edge ne-profile with X-mode have been developed.

Regarding *diagnostic developments*, a software tool to simulate O/X mode reflectometry has been developed. Results show that toroidal magnetic ripple plays a crucial role in X-mode reflectometry. A correction of the position of first plasma layer (derived from the first X-mode cutoff frequency) of about 1 cm was estimated. The reliability and accuracy of plasma position measurements has been assessed with a dedicated numerical workbench.

Concerning *modelling*, unidirectional transparent signal injection in electromagnetic codes has been modelled.

*Physics studies* on the impact of type I and type III ELMs on the plasma edge density, MHD and turbulence were carried out in 2004.

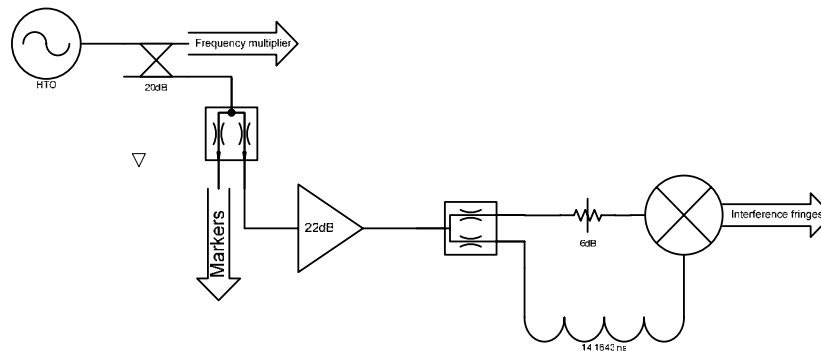


Figure 4.1 – Circuit for detailed dynamic frequency calibration using a millimetre wave delay line

<sup>1</sup> Work carried out in collaboration with the ASDEX-Upgrade Team. Contact Person: G. Conway.

<sup>2</sup> ASDEX-Upgrade is a tokamak of the Association EURATOM/IPP

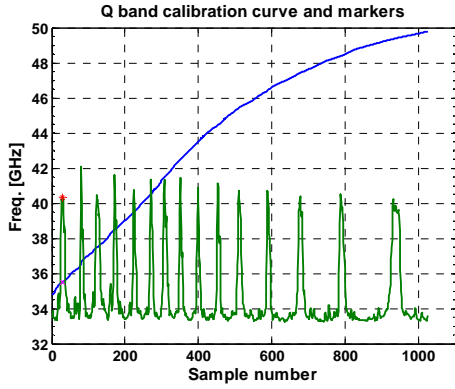


Figure 4.2 – Dynamic frequency calibration curve

#### 4.2.2. Numerical studies for plasma position

In order to test the robustness of position measurements to plasma turbulence, density perturbations were added to the  $n_e$ -profiles:

$$\delta n_e(r) = \sum_{i=1}^n a_i \cos(i \Delta k \cdot r + \varphi_i) \quad (4.1)$$

where  $a_i$  and  $\varphi_i$  are, respectively, amplitude and phase of the density fluctuations with a wave number  $k=i\Delta k$ .

Three levels of density fluctuations were investigated: rms amplitudes of 1.5%, 3%, and 5% of a density ( $n_{sep}=2 \times 10^{19} \text{ m}^{-3} \approx 25\% n_{e,med}$ ) slightly above the corrected separatrix density found for this profile. The rms position errors at densities  $n_e = 1, 1.62$  and  $3 \times 10^{19} \text{ m}^{-3}$  were less than 5 mm for single sweep profiles while in burst mode

analysis (grouping of several sweep samples) were significantly reduced  $err_{rms} < 1-2 \text{ mm}$  (Figure 4.4). Errors also diminish for higher densities ( $n_e = 3 \times 10^{19} \text{ m}^{-3}$ ,  $err_{rms} < 1 \text{ mm}$ ) with burst mode analysis.

Three initial positions were simulated: the standard limiter, limiter-3 cm, and limiter+3 cm. Figure 4.3 shows the position errors at densities  $n_e = 1.6$  and  $3 \times 10^{19} \text{ m}^{-3}$  for simulated profiles with 5% turbulence level using burst analysis (8 sweeps). The absolute errors are, in all cases, below 1 cm, and decrease for higher densities. In the LFS the errors are smaller than in the HFS due to the higher proximity to the limiter and to the steepness of the profiles.

#### 4.2.3. Modelling<sup>3</sup>

A novel numerical signal injection technique has been developed allowing unidirectional injection of a wave in a wave-guiding structure, applicable to 2D finite-difference time-domain electromagnetic codes, both Maxwell and wave-equation. The reflected or backscattered waves (returned) are separated from the probing waves allowing direct access to the information on amplitude and phase of the returned wave (Figure 4.5). It also facilitates the signal processing used to extract the phase derivative (or group delay) when simulating radar systems.

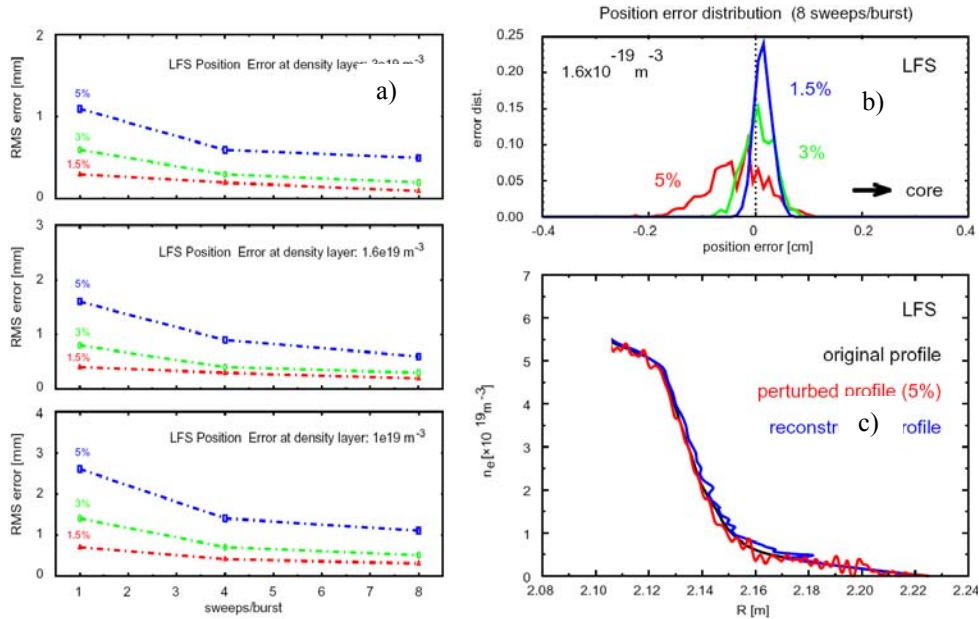


Figure 4.3 – Position error for density layers  $1.0, 1.6$  and  $3.0 \times 10^{19} \text{ m}^{-3}$  of LFS H-mode profile. Left: position error versus the number of sweeps per burst. Three layers and three levels of simulated turbulence (1.5%, 3% and 5% of  $n_{sep}$ ) are considered. On the top right, the position error distribution at density layer  $1.6 \times 10^{19} \text{ m}^{-3}$  for 8 sweeps/burst and three levels of turbulence.

<sup>3</sup> Work carried out in collaboration with Dr. S. Heurax (Université Poincaré, Nancy, France)

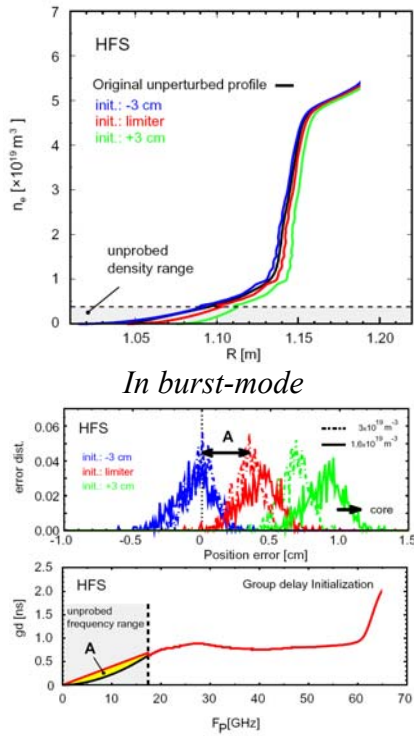


Figure 4.4 - Position error resulting from turbulence and initialization error. The original profile was initialized at three locations: the inner limiter (its original position) and 3 cm before and after the limiter. The non probed group delay was approximated linearly and its difference to the original is responsible for the shift ( $A$ ) of the distribution. The distribution was calculated for density layers  $1.6$  and  $3.0 \times 10^{19} \text{m}^{-3}$  and  $5\%$  turbulence level.

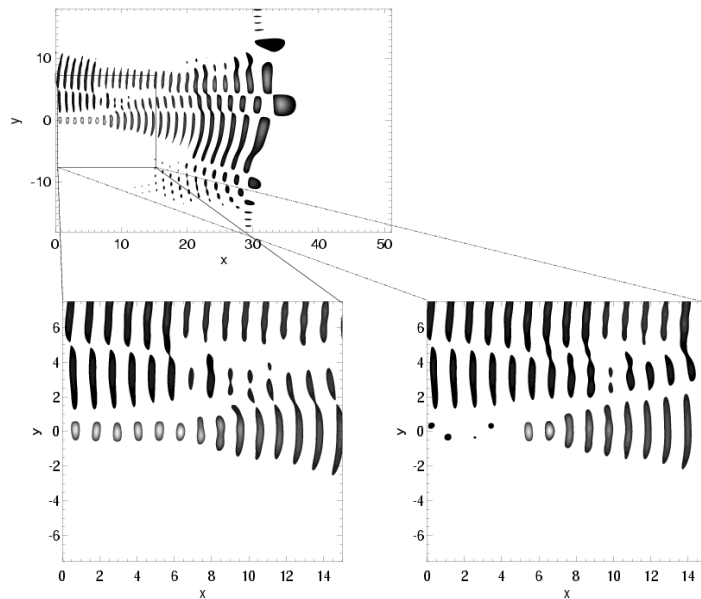


Figure 4.5 - the electric field structure close to an instant where the destructive interference occurs, is shown using an usual source (left) and an Unidirectional Transparent Source (UTS) (right). With an UTS the minute signal structures can be localized while they become completely masked when the UTS is not used.

#### 4.2.4. Study of the impact of type I and type III ELMs on the plasma edge density profiles

From the analysis of the density profile evolution during an ELM event, three characteristic phases of the ELM can be defined: precursor, collapse and recovery both at the LFS and HFS. At the collapse phase, coincident with the period of enhanced MHD activity, the crash of the density profile is observed. After the collapse of the density, the pedestal-top has moved inwards while the density profile at the scrape-off layer (SOL) broadens defining a radial pivot point localized very close and inside the separatrix, (Figure 4.6) where  $t = 0$  at the onset of the ELM.

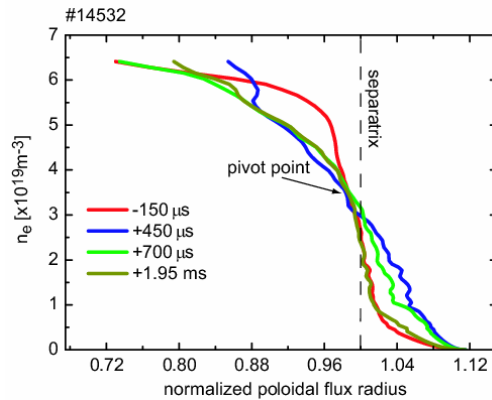


Figure 4.6 – Time evolution of the density profiles before and after an ELM event.

The two plasma regions, inside and outside the pivot point, are observed to behave differently during the recovery phase. Inside, the recovery time decreases with the ELM frequency ( $f_{ELM}$ ) and is independent of the plasma parameters; outside, the recovery time is approximately constant, independently in particular of  $f_{ELM}$ , (Figure 4.7).

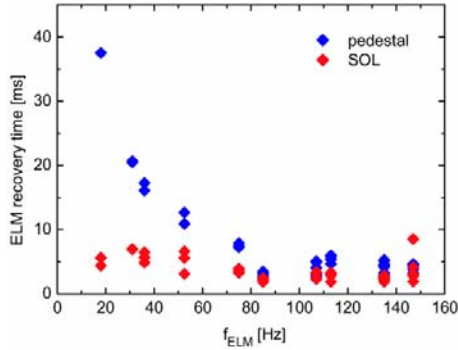


Figure 4.7 – Pedestal and SOL recovery time as a function of the ELM period.

The radial extent of the ELM perturbation, ELM affected depth (ELMAD), on the density profiles within the region of closed flux lines was determined by using the density profile before and after the ELM. ELMAD is given by the distance between the pivot point and the inner radial point (A and B, respectively, in Figure 4.8).

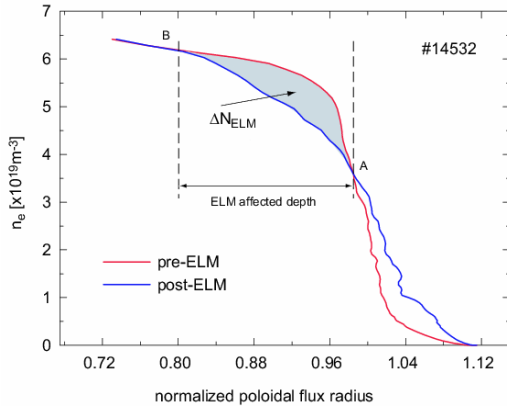


Figure 4.8 – The radial extent of the perturbation is given by the distance between the pivot point and the inner radial point where no change of the density reflected layer due to the ELM is observed (points A and B respectively). The region where the particles losses,  $\Delta N_{ELM}$  are determined is also defined by these two points.

It is found that the ELMAD normalised to the plasma minor radius, at the LFS, decreases slightly with the pedestal density (normalised to the Greenwald density) (Figure 4.9(a)). The ELM perturbation affects the outermost 10-20 cm (20-40% of the plasma minor radius), as it is also observed at JET, DIII-D and JT-60U. In AUG it is found that the ELMAD is correlated with the ELM particle losses,

$\Delta N_{ELM}$  and weakly dependent on the plasma parameters (Figure 4.9(b)).

The average radial velocity  $\langle v_r \rangle$  at which the density profiles collapse can be determined as the maximum radial displacement of a density layer over the time elapsed to reach this maximum. Figure 4.10 shows the absolute value of  $\langle v_r \rangle$  as a function of  $\Delta r = r - r_{sep}$  where each curve represents one ELM; it increases for density layers situated farther away from the pivot point.

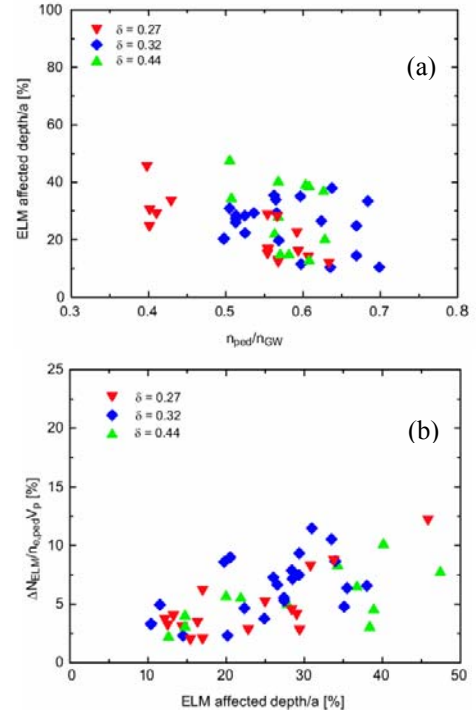


Figure 4.9 – (a) ELM affected depth normalised to the plasma minor radius as a function of the normalised pedestal density,  $n_{ped}/n_{GW}$  for the low-field side. A slight decrease of the ELM affected depth with density is observed. (b) ELM particle losses as a function of the ELM affected depth. A correlation between both is observed.

#### 4.2.5. ELM frequency control by pellet injection and magnetic triggering

In AUG, full ELM control is achieved with the increase of the ELM frequency ( $f_{ELM}$ ) by increasing the pellet frequency ( $f_{pel}$ ). Injection of small size cryogenic Deuterium pellets (at rates up to 83 Hz) imposed persisting ELM control without significant fuelling, well inside type-I ELM regime. ELM pace making was realized with the driving frequency ranging from 1.5 to 2.8 times the intrinsic ELM frequency ( $f_{ELM}^0$ ). ELM frequency enhancement by pellet pace making causes much less confinement reduction. Moreover for pellet triggered ELMs the energy loss per ELM reduces with increasing  $f_{ELM}$ .

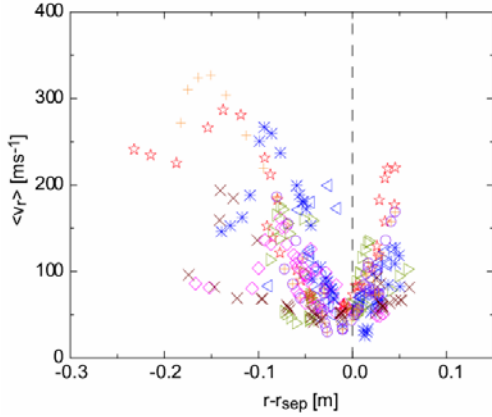


Figure 4.10 – Average radial velocity as a function of plasma position, where  $r - r_{\text{sep}} = 0$  is the position of the separatrix. Each curve represents one ELM.

#### 4.2.6. Dynamics of intrinsic and pellet triggered ELMs

FM-CW reflectometry diagnostic was used in broadband operation to study the evolution of density profiles with a very high temporal resolution during ELM phases (intrinsic and triggered ELMs). It was found that intrinsic and triggered ELMs have similar characteristics. With fixed frequency operation of the reflectometry system, the level of density fluctuations could be monitored. Adjusting the launching frequency to reflect from a plasma layer inside the steep gradient region (external transport barrier), an excellent monitor of the ELM instability was available. It was possible to characterize the turbulence footprints of intrinsic and pellet triggered ELMs, which show a very similar behavior. Thus, apart from the trigger mechanism both types of ELMs are obviously stamped by the same underlying physics and cannot be distinguished by their dynamics (Figure 4.11).

#### 4.2.7. Magnetic triggering

An alternative technique to trigger ELMs was tested, based on a rapid vertical movement of the plasma column. The observed effect of locking the ELM time sequence with plasma oscillation is attributed to an edge current induction during the vertical movement in a spatially inhomogeneous single-null vacuum configuration. This method, used on TCV<sup>4</sup>, has been adapted on AUG for type-I ELMy H-modes in the same discharges applied for the pellet approach (Figure 4.12). Shaking the plasma (“wobbling”) showed an immediate impact on the ELM behavior and once steady state conditions are reestablished locking of the ELMs to the motion with a driving frequency ( $f_D$ ) could be achieved. In first proof-of-principle experiments an operational range of  $f_D/f_{\text{ELM}}^0 = 0.75 \div 1.8$  was obtained. Again, as in the pellet case, similar characteristics were found between intrinsic and triggered type-I ELMs (Figure 4.13).

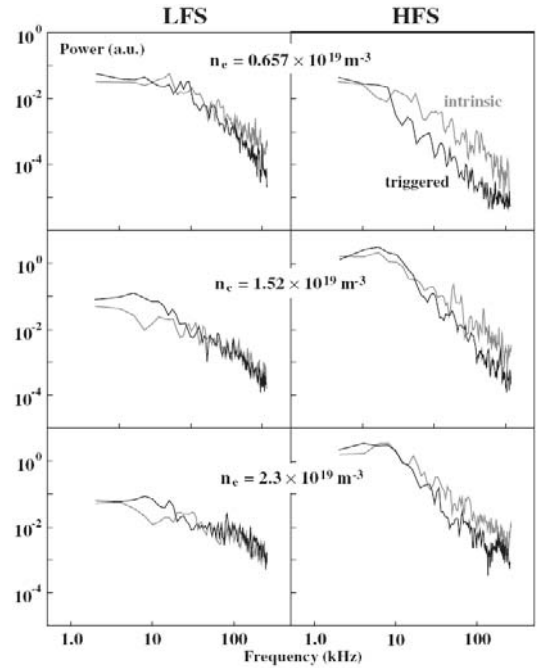


Figure 4.11 - Frequency power spectra obtained from reflectometry signals for reflected layer in the transport barrier region at different  $n_e$  values both for plasma HFS and LFS. Spectra derived from data in time windows, with duration 2.5 ms, including an intrinsic (grey) or pellet-triggered (black) ELM.

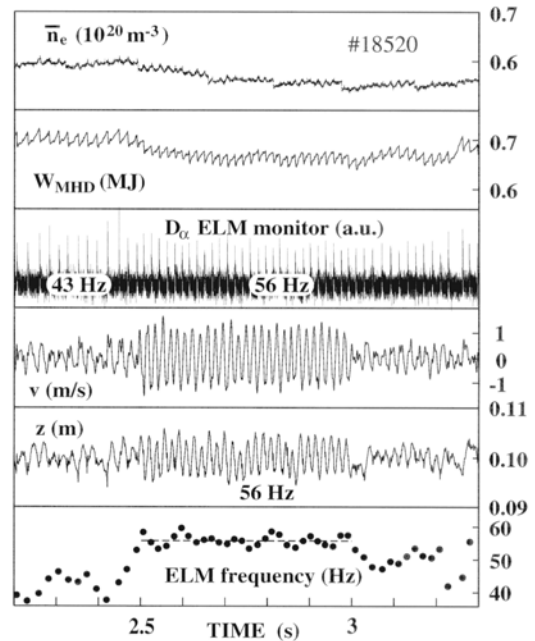


Figure 4.12 - Demonstration of magnetic ELM triggering in a type-I ELMy H-mode. The ELM frequency is raised and locks to the frequency of imposed vertical (position  $z$ ,  $v = dz/dt$ ) movement of the plasma column. During the driving phase (2.5-3.0 s) only a modest effect on particle and energy confinement is found.

<sup>4</sup> TCV is a tokamak of the Association EURATOM/Suisse Confederation

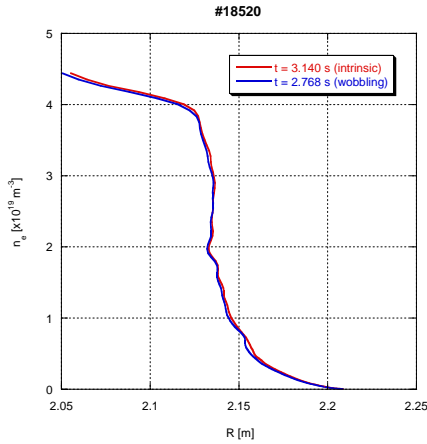


Figure 4.13 - LFS reflectometry density profiles: comparison between intrinsic and magnetic triggered ELM.

### 4.3. STUDIES ON MHD, TURBULENCE AND TRANSPORT

#### 4.3.1. Effect of Electron Cyclotron Current Drive (ECCD) on Alfvén Eigenmodes on AUG

Figure 4.14 presents the influence of ECCD on the TAE amplitude in a discharge with a constant level of ICRH power (5MW) and 1.5 MW of ECCD switched on at  $t=2.0$  s. Without ECCD, two TAE modes are observed with frequencies around 300-350 kHz and the TAE are frequently interrupted by sawteeth. By applying ECCD the TAE amplitude increases, as measured by the Mirnov probes and the TAE survive most of the sawtooth period. A third mode can also be seen during the ECCD phase. Therefore, ECCD has a slight destabilizing effect on the TAE, probably caused by a different TAE damping, due to changes in the q-profile.

#### 4.3.2. Code development for the analysis of turbulence and transport in the SOL of AUG

The model behind the GEM3 code was extended to treat the locations where the magnetic field lines intersect the material limiter/divertor plates and the plasma faces those components. Debye sheath physics concepts were used to model such interactions. The results revealed the dominance of a convective cell mode ( $k_{\parallel} = 0$ ) whenever the limiter was included, i.e., whenever the SOL boundary conditions were applied (Figure 4.15), in accordance with the experimental observations for the SOL region. The turbulent transport values were also found to increase as the large scale interchange dynamics became dominant, due to the absence of the adiabatic response of the electrons in the convective cell mode.

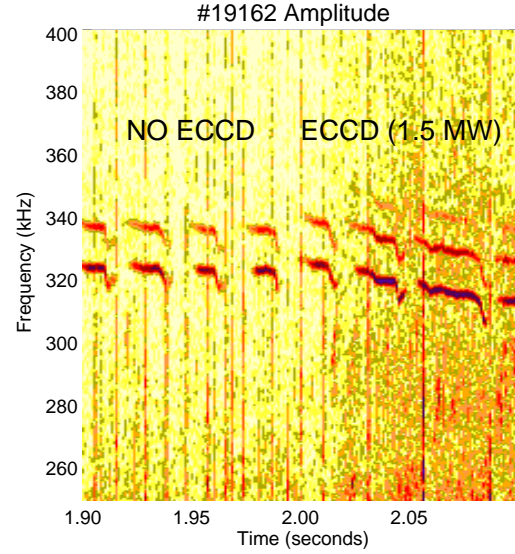


Figure 4.14 – Evolution of the AE frequency of the AE showing the effect of ECCD on the TAE amplitude

Conversely, with closed field lines boundary conditions, the field line connection in sheared magnetic field suppresses the convective cell mode, leaving the drift wave character typical of the plasma edge.

The effect of the AUG diverted geometry was investigated by performing turbulence simulations near the magnetic separatrix on a typical equilibrium magnetic field. In the region inside the magnetic separatrix, using closed flux surfaces boundary conditions, the results obtained revealed a reduction of the measured ExB turbulent transport (Figure 4.16). This result supports the scenario whereby the local magnetic shear facilitates the nonlinear decorrelation processes by twisting the turbulent perpendicular vortical structures, which are then torn apart to smaller scales. These results also stress the importance of using faithful descriptions of the tokamak geometry.

The joint effect of both the Debye sheath boundaries and the realistic geometry was also investigated. The results obtained in this case showed differences in the mode structure when the resolution of the computational grid was improved. This study revealed that the spatial scales resolution is a critically issue to cope with the poloidal dependence of the perpendicular metric components in ExB turbulence.

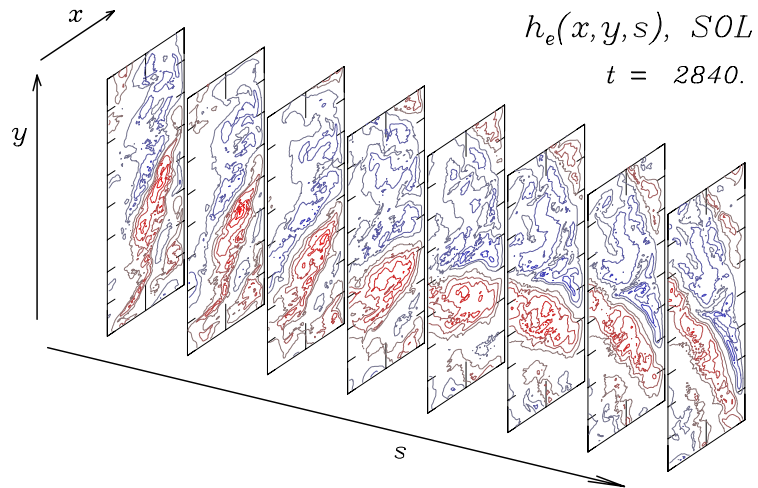


Figure 4.15 - Spatial morphology of the full computational domain of the nonadiabatic density ( $\tilde{h}_e = \tilde{\phi} - \tilde{n}_e$ ) for the SOL situation (Debye sheath model), showing the largescale, field line following convective cell ( $k_{\parallel} = 0$ ) “streamer” mode, now allowed by the geometry to exist

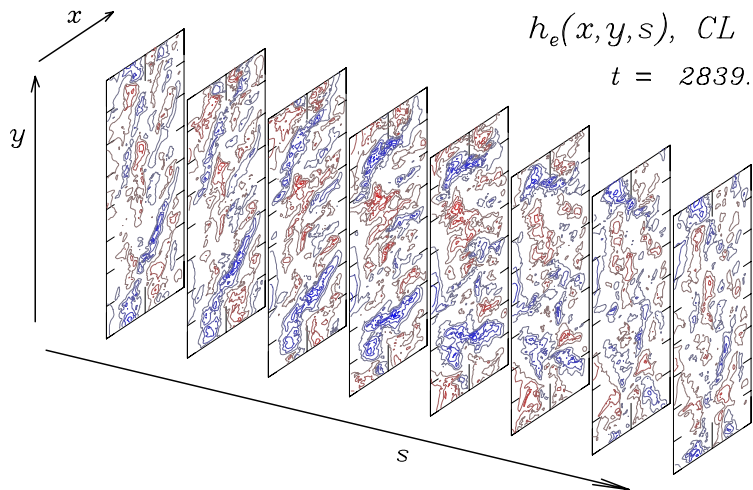


Figure 4.16 - Same as figure 1 for closed flux surfaces (CL). Note the absence of the  $k = 0$  mode he  $k = 0$  mode.